

PHANGS-JWST First Results: Multi-wavelength view of feedback-driven bubbles (The Phantom Voids) across NGC 628

ASHLEY. T. BARNES ^{1,2}, ELIZABETH J. WATKINS ³, SHARON E. MEIDT ⁴, KATHRYN KRECKEL ³, MATTIA C. SORMANI ⁵, ROBIN G. TRESS ⁶,
SIMON C. O. GLOVER ⁵, FRANK BIGIEL ⁷, RUPALI CHANDAR ⁸, ERIC EMSELLEM ^{2,9}, JANICE C. LEE ¹⁰, ADAM K. LEROY ^{11,12},
KARIN M. SANDSTROM ¹³, EVA SCHINNERER ¹⁴, ERIK ROSOLOWSKY ¹⁵, FRANCESCO BELFIORE ¹⁶, GUILLERMO A. BLANC ^{17,18},
MÉDÉRIC BOQUIEN ¹⁹, JAKOB DEN BROK ¹, YIXIAN CAO ²⁰, MÉLANIE CHEVANCE ^{5,21}, DANIEL A. DALE ²², OLEG V. EGOROV ³,
COSIMA EIBENSTEINER ²³, KATHRYN GRASHA ^{24,25}, BRENT GROVES ²⁶, HAMID HASSANI ¹⁵, JONATHAN D. HENSHAW ^{27,14},
SARAH JEFFRESON ²⁸, MARÍA J. JIMÉNEZ-DONAIRE ²⁹, BENJAMIN W. KELLER ³⁰, RALF S. KLESSEN ^{5,31}, ERIC W. KOCH ³²,
J. M. DIEDERIK KRUIJSSEN ²¹, KIRSTEN L. LARSON ³³, JING LI ³, DAIZHONG LIU ²⁰, LAURA A. LOPEZ ^{11,12,34}, ERIC J. MURPHY ³⁵,
LUKAS NEUMANN ¹, JÉRÔME PETY ^{36,37}, FRANCESCA PINNA ¹⁴, MIGUEL QUEREJETA ²⁹, FLORENT RENAUD ³⁸, TOSHIKI SAITO ³⁹,
SUMIT K. SARBADHICARY ^{11,12}, AMY SARDONE ⁴⁰, ROWAN J. SMITH ⁴¹, SOPHIA K. STUBER ¹⁴, JIAYI SUN ^{42,43}, DAVID A. THILKER ⁴⁴,
ANTONIO USERO ²⁹, BRADLEY C. WHITMORE ⁴⁵ AND THOMAS G. WILLIAMS ^{46,14}

(Received October, 2022; Revised -, 2021; Accepted December 5, 2022)

ABSTRACT

We present a high-resolution view of bubbles within The Phantom Galaxy (NGC 628); a nearby (~ 10 Mpc), star-forming ($\sim 2 M_{\odot} \text{ yr}^{-1}$), face-on ($i \sim 9^{\circ}$) grand-design spiral galaxy. With new data obtained as part of the PHANGS-*JWST* treasury program, we perform a detailed case-study of two regions of interest, one of which contains the largest and most prominent bubble in the galaxy (The Phantom Void; over 1 kpc in diameter), and the other being a smaller region that may be the precursor to such a large bubble (The Precursor Phantom Void). When comparing to matched resolution $H\alpha$ observations from the Hubble Space Telescope (*HST*), we see that the ionized gas is brightest in the shells of both bubbles, and is coincident with the youngest (~ 1 Myr) and most massive ($\sim 10^5 M_{\odot}$) stellar associations. We also find an older generation (~ 20 Myr) of stellar associations is present within the bubble of The Phantom Void. From our kinematic analysis of the HI , H_2 (CO) and HII gas across The Phantom Void, we infer a high expansion speed of around 15 to 50 km s^{-1} . The large size and high expansion speed of The Phantom Void suggest that the driving mechanism is sustained stellar feedback due to multiple mechanisms, where early feedback first cleared a bubble (as we observe now in The Precursor Phantom Void), and since then SNe have been exploding within the cavity, and have accelerated the shell. Finally, comparison to simulations shows a striking resemblance to our *JWST* observations, and suggests that such large-scale stellar feedback-driven bubbles should be common within other galaxies.

1. INTRODUCTION

High-mass stars ($> 8 M_{\odot}$) are fundamental in driving the evolution of galaxies, due to the large amounts of energy and momentum (i.e. stellar feedback) that they inject into the interstellar medium (ISM) during their short lifetimes (e.g. Krumholz et al. 2014). At early times (< 5 Myr), feedback in the pre-supernova (pre-SN) stages of high-mass stars (i.e. within HII regions) plays a critical role disrupting molecular clouds and forming bubbles within the ISM (e.g. Dale et al. 2012, 2013; Raskutti et al. 2016; Gatto et al. 2017; Rahner et al. 2017, 2019; Kim et al. 2018, 2021b; Kannan et al. 2020; Jeffreson et al. 2021; Grasha et al. 2018, 2019; Chevance et al. 2022a; McLeod et al. 2021; Barrera-

Ballesteros et al. 2021a,b; Barnes et al. 2021; Hannon et al. 2019, 2022; Barnes et al. 2022). At later times, these bubbles can merge (Clarke & Oey 2002; Simpson et al. 2012; Krause et al. 2015), and feedback from supernovae (SNe) can further act to drive expansion, forming so-called (super-)bubble structures with scales of 10s to 1000s of pc over timescales of 10s of Myr (e.g. McKee & Ostriker 1977; Mac Low & McCray 1988; Oey & Clarke 1997; Weisz et al. 2009a,b; Keller et al. 2014, 2015, 2016; Kruijsen et al. 2019; Chevance et al. 2020, 2022b; Kim et al. 2021a, 2022; Nath et al. 2020; Bagevakos et al. 2011; Orr et al. 2022; Zucker et al. 2022), even driving fountains out of the galactic plane (e.g. Veilleux et al. 2005; Fraternali 2017).

With the advent of the *JWST*, we can now, for the first time, achieve the resolution, sensitivity and coverage for an unprecedented view of bubble populations within galaxies beyond the Milky Way and the Local Group. Specifically, the

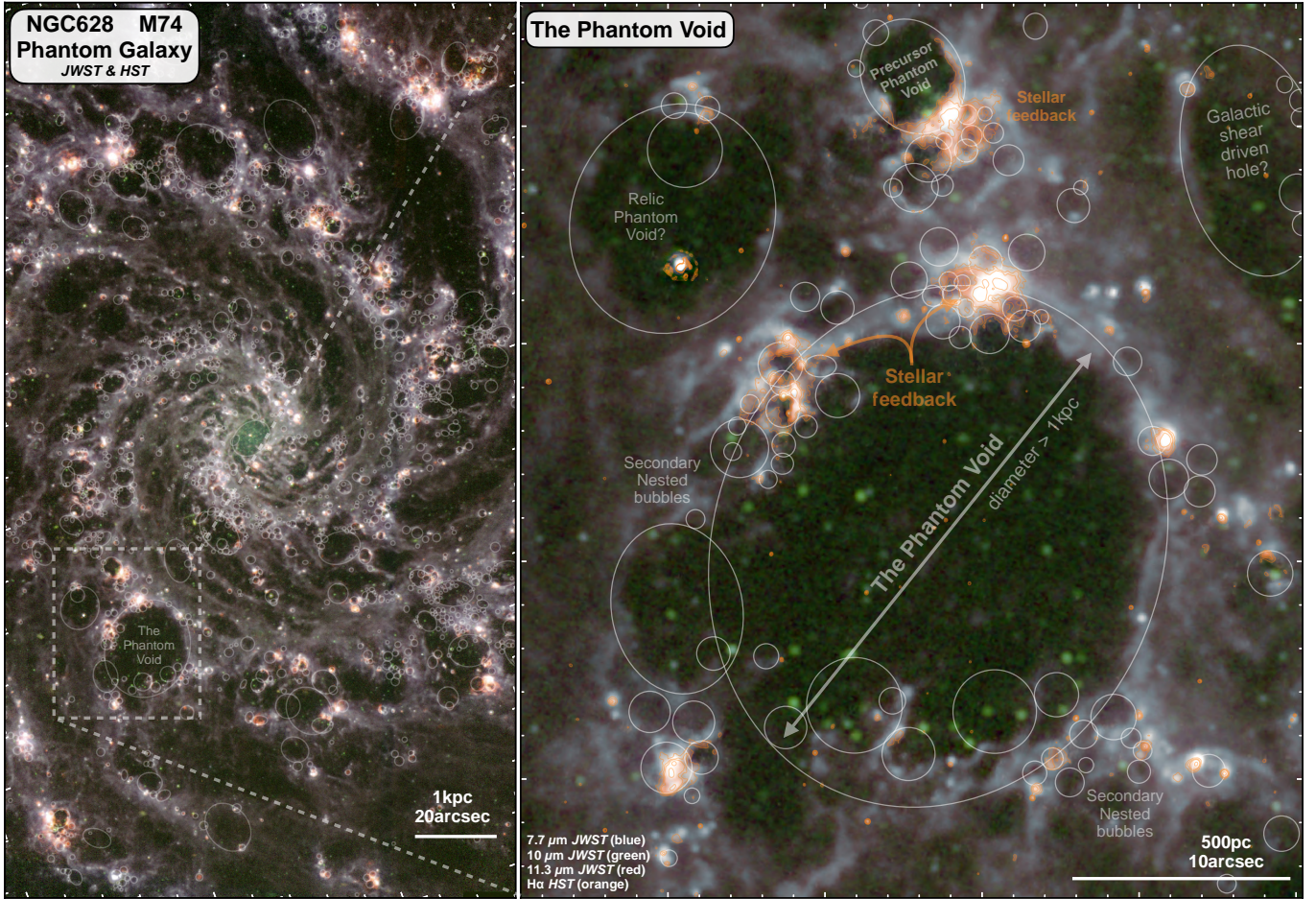


Figure 1. The prominent bubble structures across The Phantom Galaxy (Messier 74 or NGC 628). In all panels, we show an image produced from the 770W (blue), 1000W (green), and 1130W (red) band filters from the *JWST* (Lee et al. in prep), and overlaid in orange is the continuum subtracted *HST*-H α . The faded circles and ellipses show the positions of the bubbles from Watkins et al. (subm.).

wavelength coverage of MIRI is perfectly suited to this task, as it is sensitive to several polycyclic aromatic hydrocarbon (PAH) emission features (e.g. at $7.7\mu\text{m}$; see Smith et al. 2007; Draine & Li 2007; Li 2020). Emission from PAHs is particularly useful in tracing the shells of feedback-driven bubbles (e.g. Pineda et al. 2022), due to (a) the increased gas densities found in swept-up shells (PAHs are generally well mixed with the gas and illuminated by the average ISRF such that they trace the gas column very sensitively; e.g. Regan et al. 2006; Leroy et al. 2013; Chown et al. 2021; Gao et al. 2022; Leroy et al. subm.), (b) the high number of ionizing photons emitted by the OB association powering the bubbles, leading to PAHs being destroyed in the photoionized interiors of the bubbles (e.g. Galliano et al. 2018; Egorov et al. subm.; Chasten et al. subm.a,s) and (c) the low optical depth from the shell interior to the edge, which will allow FUV photons to easily heat the small dust grains (e.g. Draine & Li 2007; Draine 2011; Hensley & Draine 2021). Together, these cause the edges of bubbles to appear with high contrast against their

interior PAH emission (e.g. Churchwell et al. 2006; Watson et al. 2008).

In a companion paper in this issue, Watkins et al. (subm.) used a combination of *JWST* and *HST* observations to study the bubble population across the nearby (9.84 ± 0.63 Mpc; Anand et al. 2021a,b), star-forming ($1.8 \pm 0.5 M_{\odot} \text{ yr}^{-1}$), face-on ($i \sim 9^{\circ}$; Lang et al. 2020 and also see Blanc et al. 2013), massive ($M_{*} = 10^{10.3} M_{\odot}$, $M_{\text{HI}} = 10^{9.7} M_{\odot}$, $M_{\text{H2}} = 10^{9.4} M_{\odot}$; Walter et al. 2008; Querejeta et al. 2015; Leroy et al. 2019, 2021a), spiral galaxy Messier 74 (also known as NGC 628 and The Phantom Galaxy). These authors manually identify bubbles using a combination of $7.7\mu\text{m}$ *JWST*-MIRI observations (Lee et al. subm.), *B*-band (438 nm) PHANGS-*HST* observations (Lee et al. 2022), and VLT-MUSE H α observations (Emsellem et al. 2022). For each bubble, Watkins et al. (subm.) fit circular or elliptical apertures to the bubble boundaries (i.e. the shells) seen within this multi-wavelength dataset, and in doing so identify ~ 1700 bubbles with radii ranging between 6 and 500 pc (e.g. left panel of Fig. 1). These structures are

Table 1. Properties of The Phantom Void and The Precursor Phantom Void. Tabulated are the properties of the bubble (i.e. the ellipsoid central cavity), and shell (i.e. the ellipsoid annulus around the cavity) of each source (shown in Fig. 2). We present the central position, the semi-major and semi-minor axis length and the position angle of the ellipse used to define the outer boundary of the bubbles and shells, and, also, the mean radius of these ellipses in units of parsec. We also present the total molecular (§ 3.2.1) and atomic (§ 3.2.2) hydrogen masses and mass surface densities, and total stellar mass in young stellar associations (derived from the association catalog of Deger et al. 2020 and Larson et al. subm.; § 3.3). Lastly, we show an estimate of the expansion velocity (§ 3.2).

Property	The Phantom Void		Precursor	
	Bubble	Shell	Bubble	Shell
RA [deg]	24.1866	24.1864	24.1863	24.1863
Dec [deg]	15.7719	15.7719	15.7784	15.7782
r_{major} [arcsec]	10.8	17.6	1.7	4.9
r_{minor} [arcsec]	4.5	16.0	1.3	4.3
r_{pa} [deg]	126	126	30	30
r_{mean} [pc]	364	801	69	219
M_{H_2} [$M_{\odot}/10^5$]	12.8	379.9	3.1	38.0
M_{HI} [$M_{\odot}/10^5$]	7.0	56.4	0.2	3.5
M_{\star} [$M_{\odot}/10^5$]	1.8	7.8	1.4	1.4
Σ_{H_2} [$M_{\odot} \text{ pc}^{-2}$]	3.7	22.8	20.6	28.1
Σ_{HI} [$M_{\odot} \text{ pc}^{-2}$]	2.1	3.4	2.4	2.6
v_{exp} [km s^{-1}]	~ 20		~ 6	

clearly pervasive across the galaxy, form a complex nested structure (where smaller bubbles are preferentially located at the edges of large bubbles), and are among the most striking features in the initial *JWST* images (see Watkins et al. subm. for a in-depth discussion of the nesting of these structures and their size distributions).

In the Watkins et al. (subm.) catalog, one hole stands out due to its size (over ~ 1 kpc in diameter), circular shape, and strong contrast with respect to its environment (e.g. right panel of Fig. 1). We refer to this impressive feature as The Phantom Void, which is the focus of this letter (Tab. 1 summarizes the main properties of The Phantom Void that have been determined within this work). To help understand this structure, we also identify a nearby more compact, but still very well-defined bubble, which we call The Precursor Phantom Void and analyze in parallel (also see Tab. 1). To conduct our analysis, we combine all the datasets available taken as part of the PHANGS¹–*JWST* survey (Lee et al. subm.) and existing PHANGS multi-wavelength observations to assemble a complete panchromatic, multi-phase picture of the gas, stars, and dust in these bubbles.

2. OBSERVATIONS

2.1. PHANGS-*JWST* observations

The PHANGS (Physics at High Angular resolution in Nearby Galaxies)–*JWST* observations were taken as part of the Cycle 1 treasury project ID 02107 (Lee et al. subm.), which targets 19 nearby, star-forming galaxies with NIRCам (F200W, F300M, F335M and F360M) and MIRI (F770W, F1000W, F1130W and F2100W) imaging. The observations targeting NGC 628 cover the main star-forming disk (containing 50% of the total star formation of the galaxy), which is matched to coverage from Hubble (Lee et al. 2022), VLT-MUSE (Emsellem et al. 2022), and ALMA (Leroy et al. 2021a). We primarily make use of the F770W filter observations in this work, which have a point spread function (PSF) full width at half maximum (FWHM) of $\sim 0.25''$ (~ 12 pc at the galaxy distance). A detailed description of the complete data reduction is presented in Lee et al. (subm.).

2.2. *HST* observations

We make use of NUV–*U*–*B*–*V*–*I* band *HST* observations taken from the LEGUS survey (Calzetti et al. 2015), and reduced using the PHANGS-*HST* survey pipeline (see Lee et al. 2022). The PSF of these observations have a FWHM of ~ 0.1 – $0.2''$ (~ 5 – 10 pc). In addition, we use the narrow-band F658N map from the *HST*, to produce a higher resolution ($\sim 0.1''$) H α emission map (Proposal 10402). To do so, the F658N map is continuum subtracted using an image formed from a combination of the F814W and F550M maps, appropriately scaled using their AB zero-points (see Hannon et al. 2022 for methods).²

In this letter, we also include the properties (e.g. ages and masses; § 3.3) taken from the stellar association catalog (Deger et al. 2020; Lee et al. 2022, Larson et al. subm). The properties in this catalog were determined from SED modeling of the *HST* broadband filters with CIGALE (Boquien et al. 2019) based on the Bruzual & Charlot (2003) single stellar populations, while also including ionized gas emission (lines and continuum) and dust attenuation. We make use of the *B* band selected catalog with an association scale of 32 pc (Larson et al. subm). For this work, using a catalog selected from a different band, or association over a different scale, makes no significant difference to our results.

2.3. Ancillary observations

We also make use of continuum subtracted emission line maps (H α [OI]6300, [SII]6716) and line kinematics based on VLT/MUSE observations from the PHANGS-MUSE sur-

¹ <http://www.phangs.org>

² We are not correcting the narrow-band flux for the contribution of the [NII] emission lines. This has no impact on the results presented in this letter as we are primarily interested in the morphology of the emission rather than its absolute brightness.

vey (see [Emsellem et al. 2022](#) for a complete discussion of the processing and reduction of these observations). These provide a higher sensitivity, yet lower resolution ($\sim 1''$), view of the ionized gas compared to the *HST* $H\alpha$ map – better suited to identifying the diffuse emission within bubbles. In addition, we use CO (2-1) observations from the PHANGS-ALMA survey (see [Leroy et al. 2021a](#) for a complete description of the survey and [Leroy et al. 2021b](#) for the processing and reduction of the data), a NUV emission map from *Astrosat* (Hassani et al. in prep), a $8\mu\text{m}$ map from *Spitzer* ([Kennicutt et al. 2003](#); [Dale et al. 2009](#)), and natural weighted HI observations from the VLA (THINGS survey; [Walter et al. 2008](#)). We conduct our analysis by using a common astrometric grid, retaining the native resolution of our multi-wavelength datasets to preserve information (as opposed to smoothing to a common resolution).

3. BLOWING BUBBLES

3.1. Detailed look at feedback bubbles

[Fig. 2](#) present a detailed, multi-wavelength view of The Phantom Void and The Precursor Phantom Void regions. In The Phantom Void, we see that the main bubble is relatively devoid of any *JWST* $7.7\mu\text{m}$ emission (values of $< 1 \text{ MJy sr pix}^{-1}$) or *HST*- $H\alpha$ emission (values of $< 10^{-17} \text{ erg s}^{-1} \text{ cm}^{-1} \text{ arcsec}^{-2}$) towards the central cavity, and emission is discretely distributed around the bubble shell. We note that we use this nomenclature throughout this letter, where bubble refers to the inside cavity, while the shell refers to the perimeter with some thickness (as labeled on [Fig. 2](#)). Comparing to the broadband near-UV *HST* and *Astrosat* observations, we find that many of these emission peaks in the shell are connected to compact stellar emission sources (discussed further in [§ 3.3](#)). When comparing to the high-sensitivity, but lower resolution, PHANGS-MUSE observations, we see that there is a low level component to the diffuse $H\alpha$ emission inside of the bubble. This emission could be connected to the more diffuse emission seen in broadband *HST* and *Astrosat* observations, and is consistent with ionization by an older generation of stars (with respect to those associated with compact $H\alpha$ emission in the shell).

In contrast, The Precursor Phantom Void appears to be associated with a single star-forming complex (seen in $H\alpha$ and near-UV emission) located at the edge of the shell. Moreover, there is clear evidence from the *HST* observations that the ionizing radiation is propagating through the bubble and illuminating its far edge, which appears bright in $H\alpha$ emission. Low level $H\alpha$ is also seen in the higher sensitivity MUSE observations within the bubble cavity. Additionally, it appears that there are many more compact and less evacuated secondary bubbles towards the south of the region, which are associated with bright extended $H\alpha$ emission.

Together, the structures seen in The Phantom Void and The Precursor Phantom Void suggest that the bubbles we are seeing in the *JWST* imaging are driven by multiple generations of high-mass stars, the youngest of which are located at the bubble edges (see [§ 4](#) for a discussion of e.g. trigger star formation). These stars are then injecting their ionizing radiation into the bubble, which must have a relatively low density of hydrogen such that the radiation can propagate through the bubble and cause the diffuse $H\alpha$ emission at the dusty shell boundary. Specifically, for a characteristic ionizing photon energy of 20 eV, we expect the optical depth of a 100 pc bubble with mean atomic hydrogen density n_{H} to be approximately $\tau \sim 500 (n_{\text{H}}/\text{cm}^{-3})$, implying that n_{H} cannot be larger than $\sim 0.01 \text{ cm}^{-3}$.³ That said, The Phantom Void is even larger than this, so could have an even lower density. Indeed, The Phantom Void is so large that it is even visible as a hole within comparatively low resolution HI observations ($\sim 500 \text{ pc}$ beam; [Walter et al. 2008](#)), confirming a low atomic hydrogen density within its evacuated center (see [Fig. 2](#)). Given that the estimated HI disk scale height of NGC 628 is $\sim 800 \text{ pc}$ ([Dutta et al. 2008](#)), roughly the size of the The Phantom Void, it has likely burst out of the galaxy. Bubbles on this scale are one mechanism that could be responsible for shaping galactic-scale chimneys ([Heiles 1984](#)) and establishing gas recycling via galactic fountains (e.g. [Fraternali 2017](#)). An interesting avenue for the future would be to investigate if this cavity is filled with outflowing hot X-ray gas (e.g. with *Chandra*).

3.2. Bubble expansion

We aim to measure the expansion speed of the bubbles with a number of independent methods using our multi-wavelength datasets. These are summarized in the following subsections.

3.2.1. Molecular gas

We make two estimates of the expansion velocity from the CO (2-1) data ([Leroy et al. 2021](#)). First, we make an estimate using the line-width measured inside of the bubble, which probes the motion out of the plane (i.e. a difference between faint emission at the front and back side of the bubble). Second, we make a estimate using the velocity of the emission in the shell of the bubble, which probes the motion in the direction of the galactic plane.

In [Fig 3](#), we show the average CO (2-1) spectrum taken from inside of both bubbles, which show a weak, yet significant, signal. Here, we use a data cube that has had the local velocity field subtracted, including projected circular

³ Here we make the assumption that all the gas is atomic. However it could be possible that some of the gas is ionized, which would lower the atomic gas optical depth and allow for a higher density.

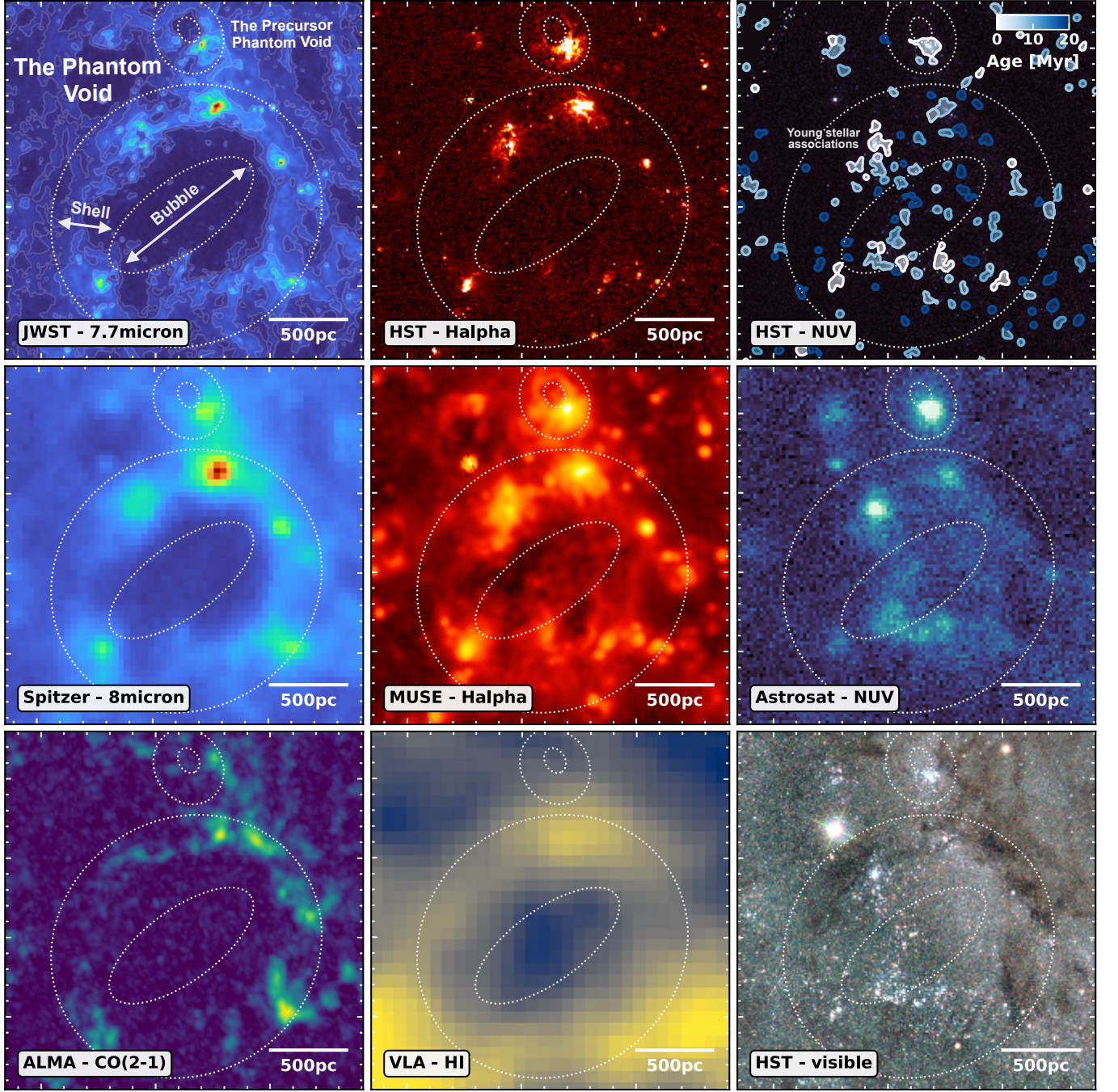


Figure 2. Comparison of a feedback-driven bubble, and its host stellar population for the Phantom Void and the Precursor Phantom Void (also shown in Fig. 1). From left to right in upper panels, we show the *JWST* 7.7 μm , *HST* $H\alpha$ and the near-UV (F275W) filters. Overlaid as colored contours on the upper right panel is the age of the stellar associations (at a scale of 32 pc; see Deger et al. 2020). From left to right in center panels are the *Spitzer* 8 μm (Dale et al. 2009), MUSE $H\alpha$ (Emsellem et al. 2022), and *Astrosat* NUV (Hassani et al. in prep) observations. In the bottom panels are the ALMA CO (Leroy et al. 2021), VLA HI (Walter et al. 2008), and *HST* broadband (Lee et al. 2022) observations. The white dashed line on all panels denotes the bubble and shell of each region (see Fig. 7). We find that young and high-mass stellar associations (< 20 Myr; $> 10^5 M_{\odot}$) exist within the bubble (particularly towards the boundaries), highlighting these as good candidates for driving the bubble expansion.

and non-circular motions, and, hence, the signal is centered on $\sim 0 \text{ km s}^{-1}$. We fit the emission with a Gaussian function, and measure a Full Width at Half Maximum (FWHM) of

31.9 km s^{-1} for The Phantom Void, and 12.1 km s^{-1} for The Precursor Phantom Void. We make the assumption that this

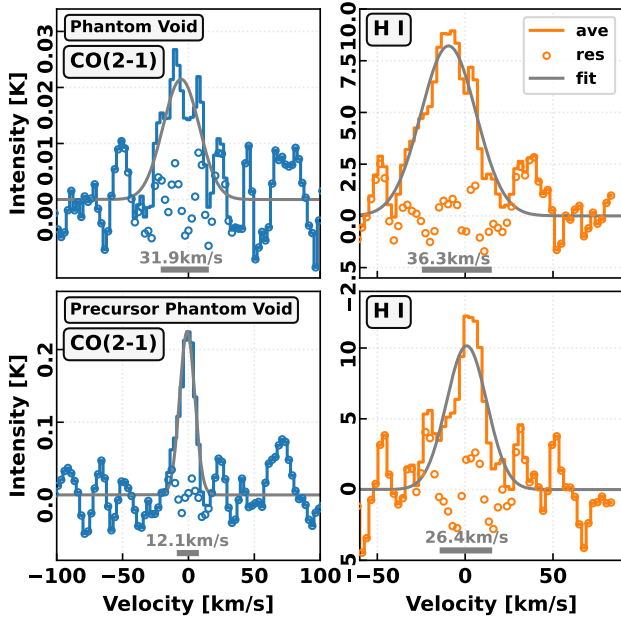


Figure 3. Spectra taken inside of the Phantom Void bubble (see Fig. 2). In the left and right panels, we present the average CO (2-1) spectrum obtained from the cube that has had the local velocity field subtracted (including rotational and non-rotational components), and the average HI spectrum, respectively. Gaussian fits to the data are overlaid as gray curves. Residuals are plotted as open points. Below each curve, we show a bar and text showing the measured FWHM (corrected for the instrument spectral resolution).

line-width is the result of the line-of-sight component of the approaching and receding side of the bubble shell.⁴ Assuming spherical expansion, then $v_{\text{exp}} = \text{FWHM}/2 \sim 16 \text{ km s}^{-1}$ for The Phantom Void and $\sim 6 \text{ km s}^{-1}$ for The Precursor Phantom Void, where the expansion velocity here is the difference in velocity between the receding and approaching side of the bubble out of the plane.

In Fig. 4, we show the molecular gas velocity field that highlights local, non-circular flows in the galactic plane at the location of The Precursor Phantom Void. Focusing on the centroid velocity of the emission around the bubble, we find that residual velocities are negative on the left side of the shell and positive on the right side of the shell. Given the orientation, rotation direction and inclination of NGC 628, this would correspond to expansion outward from the center of the bubble (i.e. the left part of the shell is moving towards a larger galactocentric radius and the right part of the shell is moving towards a smaller galactocentric radius). Specifi-

⁴ We note, however, that for large bubbles of the order of galactic scale heights, such as the Phantom Void, the bubble expansion deforms into a prolate spheroid perpendicular to the galaxy disc. This can effect the measured expansion velocity with respect to the expansion in the plane of the galaxy (e.g. see Baumgartner & Breitschwerdt 2013).

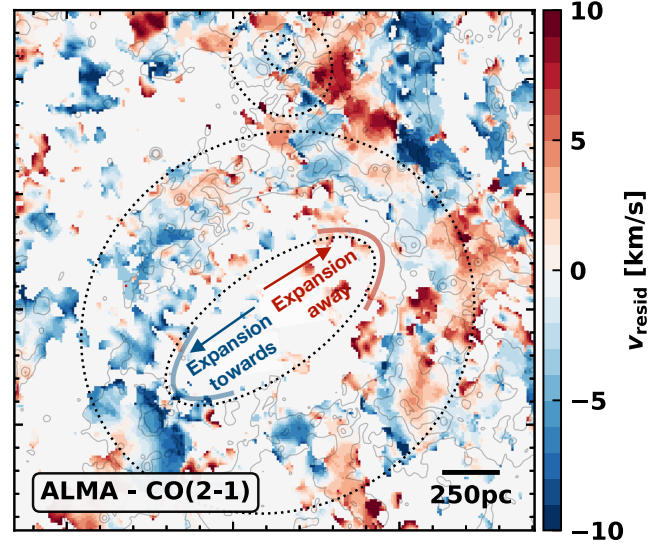


Figure 4. Residual CO velocity towards the voids. Here we show the local, non-rotational flows at the location of the phantom void, constructed from the intensity weighted centroid velocity map after subtracting the projected rotational velocity (measured by Lang et al. 2020) from each pixel. Overlaid as black contours on each panel is the $7.7 \mu\text{m}$ emission (see Fig. 2).

cally, from Fig 4, we measure v_{resid} on the left part of the bubble is $\sim -5 \text{ km s}^{-1}$, whereas on the right part of the bubble it is $+3 \text{ km s}^{-1}$, with a few positions at $+5 \text{ km s}^{-1}$. This would give $|v_{\text{resid}}| \sim 3-5 \text{ km s}^{-1}$, and hence we estimate that for The Phantom Void $v_{\text{exp}} = |v_{\text{resid}}|/\sin(i) = 20-35 \text{ km s}^{-1}$ (where $i = 8.9^\circ$; Lang et al. 2020; also see Blanc et al. 2013).

Given the simplistic assumptions on the geometry of the system, we consider that these estimates of the expansion speed perpendicular and parallel to the plane of the galaxy are consistent for the The Phantom Void. Hence the expansion velocity of the molecular gas is taken to be in the range $v_{\text{exp}} \sim 15 - 35 \text{ km s}^{-1}$. As The Precursor Phantom Void is located within the spiral arm, and due to its smaller size relative to the The Phantom Void, there is more confusion in separating the bubble from the surrounding gas within the residual velocity map. Hence, the in-plane expansion speed of The Precursor Phantom Void cannot be estimated, and we take the expansion speed estimate from the out-of-plane method: $v_{\text{exp}} \sim 6 \text{ km s}^{-1}$.

3.2.2. Atomic gas

To constrain the expansion speed in the neutral gas, we use the VLA HI (natural weighted) data cube (Fig. 2). As with the CO (2-1), we measure the averaged spectrum for the center of The Phantom Void bubble (Fig. 3 right panel), and again fit the emission with a Gaussian function. We measure a FWHM of 36.3 km s^{-1} , which is very similar to the estimate obtained from the CO (32.4 km s^{-1}). This gives a $v_{\text{exp}} = \text{FWHM}/2 \sim 18 \text{ km s}^{-1}$.

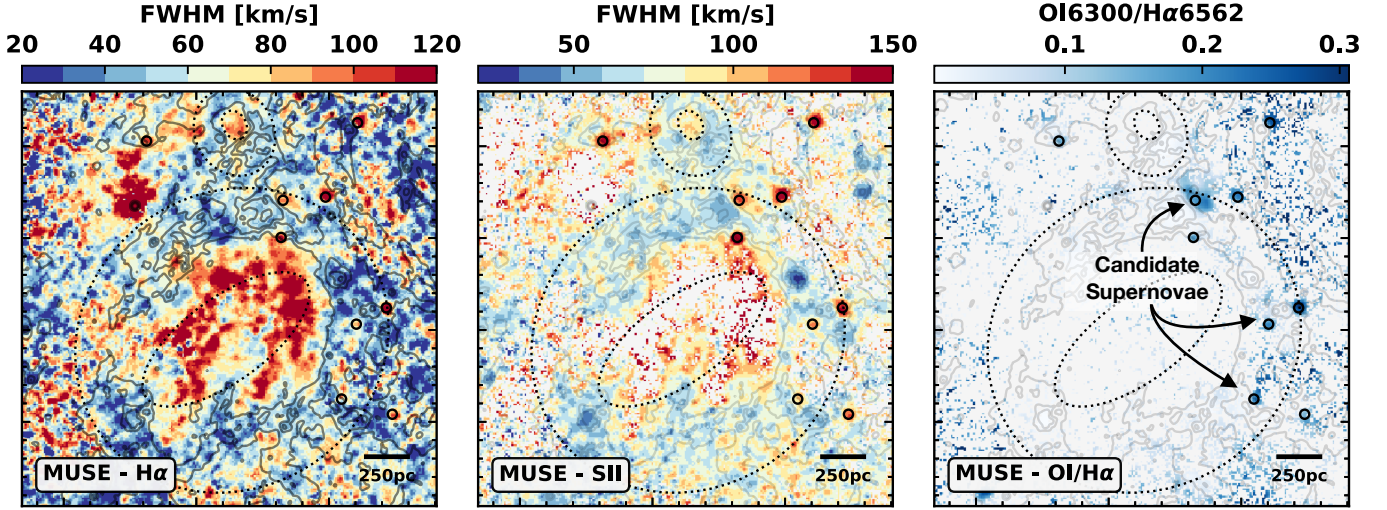


Figure 5. Evidence of stellar feedback in the ionized gas tracers towards the voids. From left to right, we show the emission-weighted velocity FWHM maps from the $H\alpha$ and the $[SII]6716$ lines, and the emission line ratio $[OI]6300/H\alpha$. Overlaid as black contours on each panel is the $7.7\mu m$ emission (see Fig. 2). We see elevated line widths distributed throughout the center of the bubble (albeit at low signal-to-noise), which we attribute to turbulence and out-of-plane expansion. Moreover, as highlighted on each panel, we see elevated line widths ($>100\text{ km s}^{-1}$) and line ratios towards the shell, which could be indicative of young supernova remnants (Li et al. in prep).

For completeness, we also estimate the atomic gas expansion speed of The Precursor Phantom Void using the same method. We measure $FWHM=26.4\text{ km s}^{-1}$, giving $v_{\text{exp}} \sim 13\text{ km s}^{-1}$. This estimate, should, however, be taken with caution, as the beam size of the VLA HI is larger than the size of The Precursor Phantom Void bubble, and, hence, could include a significant contribution from gas kinematics outside of the bubble.

3.2.3. Ionized gas

We use the MUSE $H\alpha$ emission line kinematics to constrain the expansion speed in the ionized gas (Fig 5, left panels). Across the same region used to measure the molecular and atomic expansion speeds, we find that the average FWHM for The Phantom Void is 88.4 km s^{-1} ($v_{\text{exp}} \sim 45\text{ km s}^{-1}$).⁵ Similarly, we find a FWHM for The Precursor Phantom Void of 85.1 km s^{-1} ($v_{\text{exp}} \sim 45\text{ km s}^{-1}$). These values are significantly higher than what is measured in the neutral gas ($\sim 6\text{--}20\text{ km s}^{-1}$), even when accounting for the larger thermal contribution to the FWHM of the warmer ionized medium (e.g $\sim 20\text{ km s}^{-1}$ at 10^4 K), which could highlight the fact that the ionized medium is more directly connected to the source of feedback.

Interestingly, we find systematically elevated line-widths in the interior of both bubbles relative to their shells, and even measure FWHM values of more than 100 km s^{-1} in The Phantom Void (though at these very low S/N<10 note there is

a bias towards overestimating line-widths). Such high values of the line-width could be indicative of supernova feedback contributing to increased turbulence within the center of the bubble (Egorov et al. in prep). Near the shell, we directly identify supernova remnants via their broadened $[SII]6716$ line emission and increased $[OI]/H\alpha$ line ratios (Fig. 5; Li et al, in prep). The presence of SN explosions within the shell could be contributing to continued driving of the bubble expansion (§ 3.3).

3.2.4. Galactic dynamical constraints

In the presence of differential rotation or ‘rotation curve shear’, expanding structures will become distorted over time (Palous et al. 1990). Here we use the ellipticity ϵ of shells of a given radius to place rough constraints on their expansion velocity. Assuming an isotropic bubble expansion velocity, v_{exp} , and bubble radius, $R_b = \int_0^t v_{\text{exp}} dt$ (in the absence of shear), after bubble age t , the axis ratio ($q = 1 - \epsilon$) of shearing bubbles can be written

$$q = \left(1 + \frac{dV_c}{dR} t_b\right)^{-1} = \left(1 + \frac{dV_c}{dR} \langle R_b \rangle\right)^{-1} \quad (1)$$

in terms of the rotation curve derivative dV_c/dR , the average (time-weighted) bubble radius

$$\langle R_b \rangle = \frac{\int_0^t R_b dt}{t}, \quad (2)$$

the average (time-weighted) bubble expansion velocity

$$\langle v_{\text{exp}} \rangle = \frac{R_b}{t} = \frac{\int_0^t v_{\text{exp}} dt}{t}, \quad (3)$$

⁵ The velocity dispersion shown Fig. 5 has been corrected for the instrumental velocity dispersion (Emsellem et al. 2022), and converted to the FWHM (factor of $\sqrt{8\ln(2)}$).

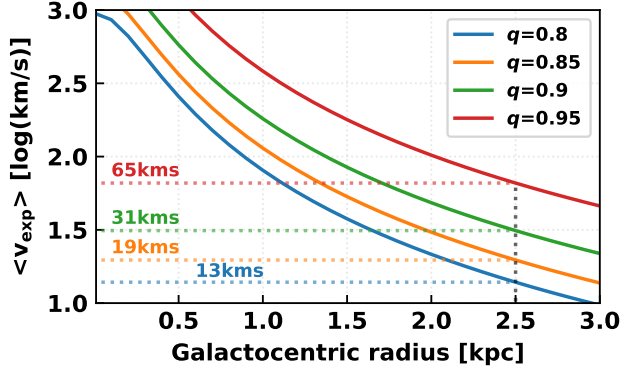


Figure 6. The expansion velocity required for Phantom Void-sized shells to retain a high degree of circularity as they expand in the presence of differential rotation at different locations in the inner disk of NGC 628. Curves show the v_{exp} required for different observed axis ratios $q=0.8$ to 0.95 (in steps of 0.05). Here a bubble radius $R_b=500$ pc is adopted and NGC 628’s rotation curve is modeled with a two-parameter fit to the measured rotation curve (Lang et al. 2020). Highlighted are the results corresponding to the approximate galactocentric radius of The Phantom Void.

(as would be estimated from the present day size and age) and effective bubble age as estimated by $t_b = \langle R_b \rangle / \langle v_{\text{exp}} \rangle = \langle R_b \rangle / R_b t$.

Using Eq. (1), the v_{exp} required to generate bubbles with a given set of average sizes and ellipticities can be determined, provided that the rotation curve is known, that is,

$$\langle v_{\text{exp}} \rangle = \frac{dV_c}{dR} \langle R_b \rangle \left(\frac{1}{q} - 1 \right)^{-1}. \quad (4)$$

Below we use this expression to obtain a basic estimate of v_{exp} under the assumption of negligible time evolution in the bubble expansion rate, such that the current bubble radius is a good approximation of $\langle R_b \rangle$. Other assumptions for the time evolution of v_{exp} will yield different results, but this should be useful for illustration purposes.⁶

The Phantom void, with a radius of $R_b \sim 500$ pc, sits at $R_{\text{gal}} \sim 2.5$ kpc and has a low ellipticity corresponding to $q \sim 0.85$. Fig. 6 shows the expansion velocities that would be required for an expanding structure with these properties to retain such a high degree of circularity. Here we have adopted an analytical two-parameter model for this galaxy’s rotation curve to estimate the rotation curve shear at all locations (Lang et al. 2020). To produce a structure like the Phantom

void, we estimate expansion velocities $v_{\text{exp}} \sim 20 \text{ km s}^{-1}$ are required.

3.2.5. Mass and energy of the shell

We use the CO (2-1) ALMA observations to estimate that there is $3.8 \times 10^7 M_\odot$ of molecular gas within the shell of The Phantom Void ($1.3 \times 10^6 M_\odot$ inside the bubble). Here we use the same shell mask shown in Fig. 2, adopt a CO (2-1)/CO (1-0) ratio of 0.61 based on direct observations (den Brok et al. 2021), and a $\alpha_{\text{CO}(1-0)} = 3.93 M_\odot \text{ pc}^{-2} (\text{km s}^{-1})^{-1}$ as predicted by empirical scaling relations (Sun et al. 2020). In addition, we estimate that there is $5.6 \times 10^6 M_\odot$ of atomic gas within the shell of The Phantom Void ($7.0 \times 10^5 M_\odot$ inside the bubble), when using the VLA data and the conversion presented in Bigiel et al. (2010).

When taking a representative expansion speed determined in the previous section of $v_{\text{exp}} \sim 20 \text{ km s}^{-1}$, we calculate that the energy required to drive a shell with this combined atomic and molecule mass is $1.7 \times 10^{53} \text{ erg}$. We find the total (HI + H₂) mass inside the shell of The Precursor Phantom Void is about ten times less than the shell ($4.2 \times 10^6 M_\odot$), which – when assuming the estimated expansion speed of $v_{\text{exp}} \sim 6 \text{ km s}^{-1}$ – implies a kinetic energy of $\sim 10^{51} \text{ erg}$.

A plausible energy source for these bubbles is stellar feedback (as discussed further in the following section). For example, a typical value for the amount of kinetic energy released per supernova is $\sim 10^{51} \text{ erg}$ (see e.g. Bethe 1990; Draine 2011), and, hence, approximately 100 SNe would be required to power The Phantom Void. On the other hand, The Precursor Phantom Void could be powered by a single SN. However, it is worth noting that this number could vary significantly depending on, for example, the contribution from pre-supernova feedback (e.g. in the form of winds, which over the lifetime of a high-mass star have been suggested to provide an energy contribution similar to a SN; e.g. Chevance et al. 2022a), and coupling efficiency of these feedback mechanisms with the expanding bubble (e.g. values of the amount of kinetic energy retained into the surrounding medium, and not radiated away, ranges between a few to a few ten percent; e.g. Thornton et al. 1998; Tamburro et al. 2009; Sharma et al. 2014; Kim & Ostriker 2015; Martizzi et al. 2015; Gentry et al. 2017). We estimate the mass of a stellar association required to produce these number of SNe assuming $f_{* \rightarrow \text{SN}} / \langle m \rangle \sim 0.01$, or that one SN is produced per $100 M_\odot$ of stars that fully populate an initial mass function (see Tamburro et al. 2009). Hence, we estimate that The Phantom Void should contain $> 10^4 M_\odot$ of stars with ages less than a few 10 Myr (i.e. the time scale for the stars to explode as SNe after they are formed), and The Precursor Phantom Void $> 10^2 M_\odot$. As we show in the following section, these criteria are fulfilled.

3.3. Stellar populations driving bubbles

⁶ For expansion that declines over time, $\langle v_{\text{exp}} \rangle$ will overestimate the present day expansion velocity. For example, in the event of an exponentially decreasing v_{exp} with time i.e. $v_{\text{exp}}(t) = v_0 e^{-t/t_0}$ with characteristic time t_0 , then when the evolution is fast and $t_0 \ll t$, the stalled radius R_b is well approximated by $\langle R_b \rangle \sim v_0 t_0 \sim R_b$ and the expansion velocity measured from eq. (4) $\langle v_{\text{exp}} \rangle = v_0 t_0 / t = R_b / t$ exceeds the present day v_{exp} but is representative of the expansion near its fastest.

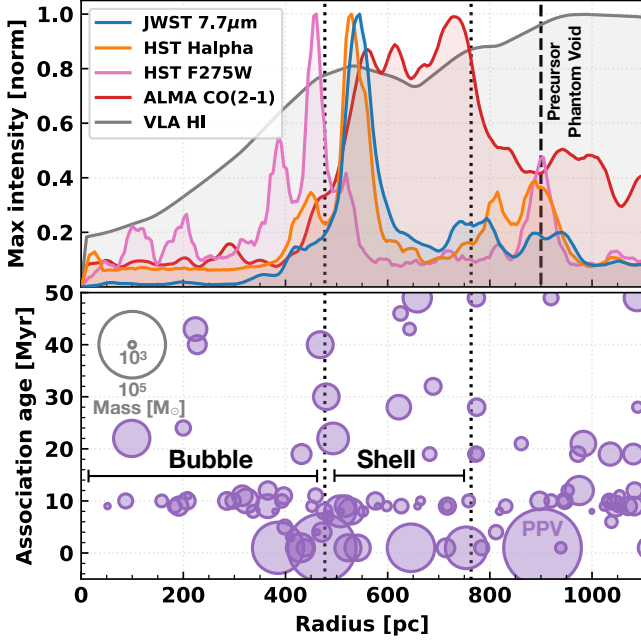


Figure 7. Distribution of intensity and stellar population in the Phantom Void (see Fig. 2). The upper panel shows the intensity distribution of the *JWST* 7.7 μm , continuum subtracted $\text{H}\alpha$ emission, *HST* NUV, ALMA CO, and VLA HI emission, as measured radially from the center of the bubble (see Fig. 2). We show the 99th percentile of the intensity in each radial bin, normalized to the value of the maximum bin (this percentile is chosen instead e.g. the mean value to better highlight where the emission distributions peak). The bottom panel shows the radial age distribution of the stellar association catalog. The size of the points indicate the mass of the stellar associations. In both panels we highlight the position of the The Precursor Phantom Void. We find evidence that younger and more higher-mass clusters are preferentially located within the shell, with respect to inside the bubble.

Within The Phantom Void, we find many compact and bright concentrations of NUV bright (young) stellar point sources within the shell (see *HST* F275W filter in Fig. 2), which spatially correspond to regions of bright $\text{H}\alpha$ and 7.7 μm emission. In addition, there appears to be an overabundance (with respect to a similar size interarm region adjacent to the bubble) of fainter point sources distributed throughout the bubble cavity, which is also seen as diffuse emission in the *Astrosat* NUV map.

Fig. 7 (upper panel) shows the flux distribution of the *JWST* 7.7 μm , *HST* $\text{H}\alpha$, *HST* NUV (F275W) filter, ALMA CO, and VLA HI emission maps measured radially from the center of The Phantom Void. We find a good correspondence between the 7.7 μm and $\text{H}\alpha$ emission, which both peak within the shell radius at ~ 600 pc (compare to dashed circles in Fig. 2). We also see that the *HST* NUV (F275W) emission is fainter within the bubble. Interestingly, we find that the peak in the NUV emission is at a smaller (~ 100 pc) radius to the 7.7 μm and $\text{H}\alpha$ emission, hinting that these clusters

may have already evacuated their immediate environment of dense atomic gas and ionized gas, respectively. We also see that the neutral gas tracers (CO and HI emission) are increased within the shell. The Precursor Phantom Void, on the other hand, shows a single compact cluster of point sources in the shell (again correspondent with bright $\text{H}\alpha$ and 7.7 μm emission), and very little point source emission within the bubble.

In Fig. 2 (upper right panel), we also overlay as colored contours the ages of the stellar associations (see § 2.2; Deger et al. 2020, Larson et al. subm). These indicate that the stellar associations throughout the bubble and shell are generally young (< 20 Myr). We estimate the total stellar mass of these young stellar associations within the The Phantom Void region to be $10^{6.0} M_{\odot}$ (80% of this stellar mass is in the shell, and 20% is in the bubble). These associations could be viable powering sources for these bubbles, either currently or, in the case of those inside the bubble of The Phantom Void, they may represent the past generation of stars that created the bubbles (§ 4).

Interestingly, several of the stellar associations are very young (< 5 Myr). Both in The Phantom Void and The Precursor Phantom Void, these associations reside in the shells (as inferred from the $\text{H}\alpha$). Indeed, Fig. 7 (lower panel) shows the radial distribution of ages from the association catalog across The Phantom Void where the size of each point indicates the stellar mass. We see evidence that there is a higher number of younger and more massive associations situated within the shell, as opposed to inside of the bubble. We find that there are 10 associations with ages less than 5 Myr within the shell of The Phantom Void, which have a maximum mass of $10^5 M_{\odot}$ (total mass of $3.2 \times 10^5 M_{\odot}$), and, therefore, are massive enough to harbor OB stars (i.e. strong sources of stellar feedback).

We consider whether the stellar population ages align with the previous estimates of the bubble expansion speed. To test this, we make a calculation of the expansion velocity based on the radius of the bubble ($R \sim 500$ pc), and the mean age of the associations within the bubble of $t \sim 10$ Myr. According to the classical Weaver et al. (1977) model of expanding bubbles, $v_{\text{exp}} \simeq 0.6R/t$ assuming they are in an adiabatic stage of their evolution. This implies $v_{\text{exp}} = 30 \text{ km s}^{-1}$, which is very close to the values estimated from our kinematic analysis (§ 3.2).

The large size, high expansion speed, and large energy required to power the The Phantom Void bubble (§ 3.2) suggests that the driving mechanism is stellar feedback, sustained by a combination of multiple mechanisms. We propose that early feedback first cleared a bubble, as we are now currently witnessing for The Precursor Phantom Void (and to some extent continue to see in the shell of The Phantom Void). Since then, SNe have been exploding within the cav-

ity, and have accelerated the shell (e.g. Keller et al. 2022). This sustained injection of energy and momentum is what is required reach high (50 km s^{-1}) expansion speeds (i.e. seen in the ionized gas), because the continuous energy input keeps the pressure in the bubble high, whereas having only a single SN would cause the pressure to drop as the bubble expands (e.g. Mac Low & McCray 1988). Finally, the star formation and SNe that are observed in the shell could further contribute to the current and future expansion of the shell.

4. STAR FORMATION AT THE BUBBLE BOUNDARIES

We have found that The Phantom Void contains a significant amount of ongoing star formation within its shell (as seen in the $H\alpha$ emission and the young, massive stellar associations), and also that this shell contains a large reservoir of molecular gas (see Tab. 1). This could then imply several physical scenarios as to why star formation is preferentially located towards the shell, of which we provide an non-exhaustive list of examples below.

- i) Gravitationally unbound gas is collected in the shell of the bubble as it expands, which then becomes dense and then star formation is triggered (i.e. gas that would not have otherwise formed stars; e.g. Elmegreen & Lada 1977; Whitworth et al. 1994).
- ii) Gravitationally bound gas either from the parent cloud, or surrounding the initial star forming region, is moved by the expansion of the bubble into the shell, which then forms stars (i.e. gas that would have otherwise formed stars, but in a different location).
- iii) If star formation proceeds sequentially in a cloud/region in an inside-out fashion, then we would naturally get the oldest stars in the middle of the cloud, with younger stars near the edge.

Differentiating between these cause and effect scenarios for the formation of the feedback-driven bubbles and future episodes of star formation is non-trivial, and has been a very long-standing problem in the Galactic star formation community. Nonetheless, below we outline methods to test this in future work.

The different cases make different predictions regarding the ages of the various young stellar clusters/associations. In scenario (i), where star formation is triggered by shell collapse, we would expect all of the young regions in the shell to have ages less than the age of the shell (and hence also less than the age of the central associations). However, this need not be the case in scenario (ii). If bound clouds are being swept-up, that are already capable of forming stars, then it is likely that some of them will already have stars when they get swept up, whereas others will not, and we would

therefore expect to see a broader distribution of ages than in scenario (i).

Another interesting test would be to look at whether there is a population of young stellar clusters/associations just inside the shell. This is what one might expect if the expanding shell sweeps away molecular clouds that have already started forming stars, as the shock will act on the gas but not the stars, which should therefore get left behind. This would be much harder to bring about in scenario (i), as in this case, we would expect that the radial outward velocity of the stars at their birth should be the same as that of their parent giant molecular clouds (i.e. they should move along with the shell, or even move out faster than the shell in the case where it is significantly decelerating). Interesting, as seen in Fig. 7, we do find that the young stars (seen in the *HST*-NUV and in the cluster association catalog) are preferentially located on the inner edge of the shell (offset from the peak in $7.7 \mu\text{m}$ emission by 50 to 100 pc).

5. ARE PHANTOM VOIDS COMMON IN GALAXIES?

The Phantom Void is one of the most striking features within the new *JWST* data, which was not as pronounced in our existing PHANGS multi-wavelength datasets. Only with the resolution and sensitivity afforded by *JWST* do such coherent, large-scale features become clearly apparent (Fig. 1). It is then interesting to consider if Phantom Voids are a common feature of other galaxies.

Watkins et al. (subm.) estimates that there should be ~ 1900 bubbles identifiable in the PHANGS-*JWST* observations per $1 \text{ M}_{\odot} \text{ yr}^{-1}$ of star formation rate (§ 3.1). Hence, using their size distribution, we expect to find ~ 1 with a radius of $\sim 500 \text{ pc}$ per $1 \text{ M}_{\odot} \text{ yr}^{-1}$ of star formation rate. This is more-or-less in line with the observations, given that the star formation rate contained within the mapped region is $\sim 1 \text{ M}_{\odot} \text{ yr}^{-1}$. Across the remaining galaxies to be mapped as part of the PHANGS-*JWST* treasury program (total $42 \text{ M}_{\odot} \text{ yr}^{-1}$), we could then expect to uncover many Phantom Voids (albeit these may be harder to identify in galaxies with higher inclinations than NGC 628, because of greater foreground confusion).

We offer a brief comparison between the new *JWST* observations and theoretical predictions/simulations. Figure 8 compares our $7.7 \mu\text{m}$ emission map and snapshots from two sets of galaxy simulations (with matched physical scales).

The first is the isolated (non-interacting) galaxy simulation from Tress et al. (2020, 2021). This simulation represents a generic isolated galaxy and is not tuned to reproduce the particular properties of NGC 628. The aim of the simulation was to study molecular clouds and their associated star formation in a galactic environment. The simulation includes a live N-body stellar and dark matter component. The ISM is modeled using a time-dependent chemical network that

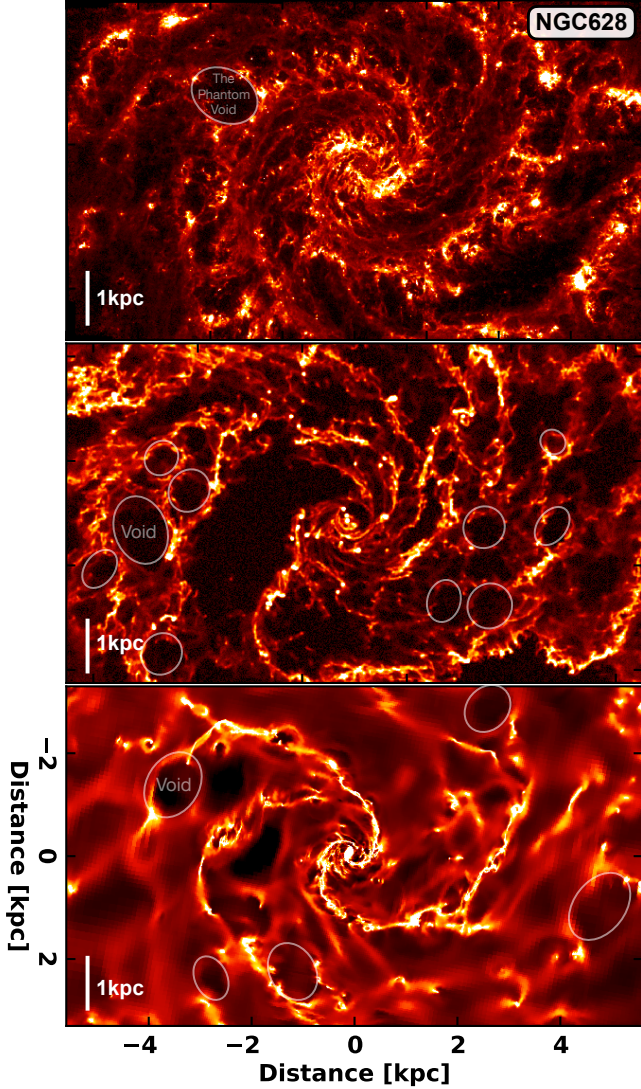


Figure 8. Phantom Voids in both observations and simulations. Shown in the upper panel is the *JWST* 7.7 μm emission map. The middle panel shows the isolated galaxy simulation from Tress et al. (2020) (the same simulation shown in the bottom panels of their Fig. 14). In color-scale is the total column density, which we expect (away from regions of active star formation), to correspond well to the 7.7 μm emission (Sandstrom et al. *subm.*; Leroy et al. *subm.*). The bottom panel shows the isolated galaxy simulation tuned for NGC 628 from Emsellem et al. (*in prep.*). We have optimized the color-scales such that both maps have a similar qualitative appearance, and the physical scales of all panels are matched. We see that large-scale ($\sim 1\text{kpc}$ -sized) voids are also common within the simulations, several of which are highlighted by the faded white ellipses.

keeps track of hydrogen and carbon chemistry, a physically motivated model for the formation of new stars using sink particles, and type Ia and type II supernova feedback. The simulation reaches sub-parsec resolution in the dense regions (see Figure 3 in Tress et al. 2020) and self-consistently follows the formation of individual molecular clouds from the

large-scale flow and their embedded star formation. More details about the simulation can be found in Tress et al. (2020).

The second simulation is a dedicated hydro-dynamical simulation of an isolated main-sequence star-forming galaxy, using known properties of NGC 628 to generate initial conditions (stellar and gas mass profiles, velocity profile, viewing angles). The simulation was run using Ramses (Teyssier 2002), an adaptive-mesh refinement code with a maximum sampling of 3.6 pc for the gas cells. It includes live particles for dark matter, old and new stars, atomic and molecular cooling, constant efficiency per free-fall time star formation above a given gas density, with recipes for UV background, feedback from type-Ia and II supernovae, radiative pressure and stellar winds.

The similarity in morphology between simulations and observations is striking. We show as ellipses in the bottom two panels of Fig. 8 several large-scale ($\sim 1\text{kpc}$ -sized) voids, similar to The Phantom Void, that have been identified in the simulations.⁷ In addition, we see many smaller bubbles in the simulations that are similar in size to The Precursor Phantom Void. Indeed, simulations have been predicting a bubble-rich ISM morphology for decades (e.g. Wada 2008; Grisdale et al. 2017), and HI observations have hinted at a similar morphology (see for example Fig. 1 in Boomsma et al. 2008). However, HI observations have limited resolution outside of the Milky Way and it is only with the advent of *JWST* that we can for the first time confirm the predictions of simulations so spectacularly. In simulations which include perturbations from satellites, such as the M51 analog shown in Pettitt et al. (2017), large-scale voids are also clear in the gas column density. The voids seen in Pettitt et al. (2017) are driven by SN feedback, and also track the edges of the spiral arms, as we see in M74. The strong similarity between observations and simulations suggests that the physical processes included in the simulations (gas self-gravity, supernova feedback, and differential rotation) are at the origin of the observed morphology. Further analysis, that is out of the scope of this paper, will be necessary to quantify in more detail the statistical properties of simulations vs observations (e.g. see Sandstrom et al. *subm.*).

6. CONCLUSIONS

This letter demonstrates the potential for new PHANGS-*JWST* observation to be used to identify (morphologically) stellar feedback powered bubbles, and highlights the need for multi-wavelength datasets to study and understand their physical properties. Here we provide a detailed case-study

⁷ We note, however, the identification procedure in the simulations not identical to the observations (which combined multiple filters). In future, we aim to make a more direct comparison based on e.g. using POLARIS to create synthetic observations of the *JWST* filters as predicted by the simulation.

support from FONDECYT regular grant 1211000 and by the ANID BASAL project FB210003. ER acknowledges the support of the Natural Sciences and Engineering Research Council of Canada (NSERC), funding reference number RGPIN-2022-03499. This research was supported by the Excellence Cluster ORIGINS which is funded by the Deutsche Forschungsgemeinschaft (DFG, German Research Foundation) under Germany's Excellence Strategy - EXC-2094-390783311. Some of the simulations in this paper have been carried out on the computing facilities of the Computational Center for Particle and Astrophysics (C2PAP). EE would like to thank Alexey Krukau and Margarita Petkova for their support through C2PAP. KG is supported by the Australian Research Council through the Discovery Early Career Researcher Award (DECRA) Fellowship DE220100766 funded by the Australian Government. KG is supported by the Australian Research Council Centre of Excellence for All Sky Astrophysics in 3 Dimensions (ASTRO 3D), through project number CE170100013. MQ acknowledges support from the Spanish grant PID2019-106027GA-C44, funded by MCIN/AEI/10.13039/501100011033. FR acknowledges support from the Knut and Alice Wallenberg Foundation. CE acknowledges funding from the Deutsche

Forschungsgemeinschaft (DFG) Sachbeihilfe, grant number BI1546/3-1 AKL gratefully acknowledges support by grants 1653300 and 2205628 from the National Science Foundation, by award JWST-GO-02107.009-A, and by a Humboldt Research Award from the Alexander von Humboldt Foundation. JS acknowledges support by the Natural Sciences and Engineering Research Council of Canada (NSERC) through a Canadian Institute for Theoretical Astrophysics (CITA) National Fellowship. SKS acknowledges financial support from the German Research Foundation (DFG) via Sino-German research grant SCHI 536/11-1.

Facilities: *HST* (Hubble Space Telescope), *JWST*, *ALMA* (Atacama Large Millimeter/submillimeter Array), *VLT-MUSE* (Very Large Telescope - Multi Unit Spectroscopic Explorer), *VLA* (The Karl G. Jansky Very Large Array), *Spitzer* space telescope, *Astrosat* (Astronomy satellite)

Software: *Astropy* (Astropy Collaboration et al. 2013, 2018, 2022), *SAOImageDS9* (Joye & Mandel 2003), *CARTA* (Comrie et al. 2021), *APLpy* (Robitaille & Bressert 2012; Robitaille 2019)
































REFERENCES

- Anand, G. S., Lee, J. C., Van Dyk, S. D., et al. 2021a, *MNRAS*, 501, 3621, doi: [10.1093/mnras/staa3668](https://doi.org/10.1093/mnras/staa3668)
- Anand, G. S., Rizzi, L., Tully, R. B., et al. 2021b, *AJ*, 162, 80, doi: [10.3847/1538-3881/ac0440](https://doi.org/10.3847/1538-3881/ac0440)
- Astropy Collaboration, Robitaille, T. P., Tollerud, E. J., et al. 2013, *A&A*, 558, A33, doi: [10.1051/0004-6361/201322068](https://doi.org/10.1051/0004-6361/201322068)
- Astropy Collaboration, Price-Whelan, A. M., Sipőcz, B. M., et al. 2018, *AJ*, 156, 123, doi: [10.3847/1538-3881/aabc4f](https://doi.org/10.3847/1538-3881/aabc4f)
- Astropy Collaboration, Price-Whelan, A. M., Lim, P. L., et al. 2022, *ApJ*, 935, 167, doi: [10.3847/1538-4357/ac7c74](https://doi.org/10.3847/1538-4357/ac7c74)
- Bagetakos, I., Brinks, E., Walter, F., et al. 2011, *The Astronomical Journal*, 141, 23, doi: [10.1088/0004-6256/141/1/23](https://doi.org/10.1088/0004-6256/141/1/23)
- Barnes, A. T., Glover, S. C. O., Kreckel, K., et al. 2021, *MNRAS*, 508, 5362, doi: [10.1093/mnras/stab2958](https://doi.org/10.1093/mnras/stab2958)
- Barnes, A. T., Chandar, R., Kreckel, K., et al. 2022, *A&A*, 662, L6, doi: [10.1051/0004-6361/202243766](https://doi.org/10.1051/0004-6361/202243766)
- Barrera-Ballesteros, J. K., Sánchez, S. F., Heckman, T., et al. 2021a, *MNRAS*, 503, 3643, doi: [10.1093/mnras/stab755](https://doi.org/10.1093/mnras/stab755)
- Barrera-Ballesteros, J. K., Heckman, T., Sánchez, S. F., et al. 2021b, *ApJ*, 909, 131, doi: [10.3847/1538-4357/abd855](https://doi.org/10.3847/1538-4357/abd855)
- Baumgartner, V., & Breitschwerdt, D. 2013, *A&A*, 557, A140, doi: [10.1051/0004-6361/201321261](https://doi.org/10.1051/0004-6361/201321261)
- Bethe, H. A. 1990, *Reviews of Modern Physics*, 62, 801, doi: [10.1103/RevModPhys.62.801](https://doi.org/10.1103/RevModPhys.62.801)
- Bigiel, F., Leroy, A., Walter, F., et al. 2010, *AJ*, 140, 1194, doi: [10.1088/0004-6256/140/5/1194](https://doi.org/10.1088/0004-6256/140/5/1194)
- Blanc, G. A., Weinzirl, T., Song, M., et al. 2013, *AJ*, 145, 138, doi: [10.1088/0004-6256/145/5/138](https://doi.org/10.1088/0004-6256/145/5/138)
- Boomsma, R., Oosterloo, T. A., Fraternali, F., van der Hulst, J. M., & Sancisi, R. 2008, *A&A*, 490, 555, doi: [10.1051/0004-6361:200810120](https://doi.org/10.1051/0004-6361:200810120)
- Boquien, M., Burgarella, D., Roehlly, Y., et al. 2019, *A&A*, 622, A103, doi: [10.1051/0004-6361/201834156](https://doi.org/10.1051/0004-6361/201834156)
- Bruzual, G., & Charlot, S. 2003, *MNRAS*, 344, 1000, doi: [10.1046/j.1365-8711.2003.06897.x](https://doi.org/10.1046/j.1365-8711.2003.06897.x)
- Calzetti, D., Lee, J. C., Sabbi, E., et al. 2015, *AJ*, 149, 51, doi: [10.1088/0004-6256/149/2/51](https://doi.org/10.1088/0004-6256/149/2/51)
- Chastenet, J., et al. subm.a, *ApJL*
- . subm.b, *ApJL*
- Chevance, M., Krumholz, M. R., McLeod, A. F., et al. 2022a, *arXiv e-prints*, arXiv:2203.09570. <https://arxiv.org/abs/2203.09570>
- Chevance, M., Kruijssen, J. M. D., Hygate, A. P. S., et al. 2020, *MNRAS*, 493, 2872, doi: [10.1093/mnras/stz3525](https://doi.org/10.1093/mnras/stz3525)
- Chevance, M., Kruijssen, J. M. D., Krumholz, M. R., et al. 2022b, *MNRAS*, 509, 272, doi: [10.1093/mnras/stab2938](https://doi.org/10.1093/mnras/stab2938)
- Chown, R., Li, C., Parker, L., et al. 2021, *MNRAS*, 500, 1261, doi: [10.1093/mnras/staa3288](https://doi.org/10.1093/mnras/staa3288)
- Churchwell, E., Povich, M. S., Allen, D., et al. 2006, *ApJ*, 649, 759, doi: [10.1086/507015](https://doi.org/10.1086/507015)

- Clarke, C., & Oey, M. S. 2002, *MNRAS*, 337, 1299, doi: [10.1046/j.1365-8711.2002.05976.x](https://doi.org/10.1046/j.1365-8711.2002.05976.x)
- Comrie, A., Wang, K.-S., Hsu, S.-C., et al. 2021, CARTA: The Cube Analysis and Rendering Tool for Astronomy, 2.0.0, Zenodo, Zenodo, doi: [10.5281/zenodo.3377984](https://doi.org/10.5281/zenodo.3377984)
- Dale, D. A., Cohen, S. A., Johnson, L. C., et al. 2009, *ApJ*, 703, 517, doi: [10.1088/0004-637X/703/1/517](https://doi.org/10.1088/0004-637X/703/1/517)
- Dale, J. E., Ercolano, B., & Bonnell, I. A. 2012, *MNRAS*, 424, 377, doi: [10.1111/j.1365-2966.2012.21205.x](https://doi.org/10.1111/j.1365-2966.2012.21205.x)
- . 2013, *MNRAS*, 430, 234, doi: [10.1093/mnras/sts592](https://doi.org/10.1093/mnras/sts592)
- Deger, S., Lee, J., Thilker, D., et al. 2020, in *American Astronomical Society Meeting Abstracts*, Vol. 235, American Astronomical Society Meeting Abstracts #235, 178.01
- den Brok, J. S., Chatzigiannakis, D., Bigiel, F., et al. 2021, *MNRAS*, 504, 3221, doi: [10.1093/mnras/stab859](https://doi.org/10.1093/mnras/stab859)
- Draine, B. T. 2011, *ApJ*, 732, 100, doi: [10.1088/0004-637X/732/2/100](https://doi.org/10.1088/0004-637X/732/2/100)
- Draine, B. T., & Li, A. 2007, *ApJ*, 657, 810, doi: [10.1086/511055](https://doi.org/10.1086/511055)
- Dutta, P., Begum, A., Bharadwaj, S., & Chengalur, J. N. 2008, *MNRAS*, 384, L34, doi: [10.1111/j.1745-3933.2007.00417.x](https://doi.org/10.1111/j.1745-3933.2007.00417.x)
- Egorov, O., et al. subm., *ApJL*
- Elmegreen, B. G., & Lada, C. J. 1977, *ApJ*, 214, 725, doi: [10.1086/155302](https://doi.org/10.1086/155302)
- Emsellem, E., Schinnerer, E., Santoro, F., et al. 2022, *A&A*, 659, A191, doi: [10.1051/0004-6361/202141727](https://doi.org/10.1051/0004-6361/202141727)
- Fraternali, F. 2017, in *Astrophysics and Space Science Library*, Vol. 430, Gas Accretion onto Galaxies, ed. A. Fox & R. Davé, 323, doi: [10.1007/978-3-319-52512-9_14](https://doi.org/10.1007/978-3-319-52512-9_14)
- Galliano, F., Galametz, M., & Jones, A. P. 2018, *ARA&A*, 56, 673, doi: [10.1146/annurev-astro-081817-051900](https://doi.org/10.1146/annurev-astro-081817-051900)
- Gao, Y., Tan, Q.-H., Gao, Y., et al. 2022, *arXiv e-prints*, arXiv:2210.01982. <https://arxiv.org/abs/2210.01982>
- Gatto, A., Walch, S., Naab, T., et al. 2017, *MNRAS*, 466, 1903, doi: [10.1093/mnras/stw3209](https://doi.org/10.1093/mnras/stw3209)
- Gentry, E. S., Krumholz, M. R., Dekel, A., & Madau, P. 2017, *MNRAS*, 465, 2471, doi: [10.1093/mnras/stw2746](https://doi.org/10.1093/mnras/stw2746)
- Grasha, K., Calzetti, D., Bittler, L., et al. 2018, *MNRAS*, 481, 1016, doi: [10.1093/mnras/sty2154](https://doi.org/10.1093/mnras/sty2154)
- Grasha, K., Calzetti, D., Adamo, A., et al. 2019, *MNRAS*, 483, 4707, doi: [10.1093/mnras/sty3424](https://doi.org/10.1093/mnras/sty3424)
- Grisdale, K., Agertz, O., Romeo, A. B., Renaud, F., & Read, J. I. 2017, *MNRAS*, 466, 1093, doi: [10.1093/mnras/stw3133](https://doi.org/10.1093/mnras/stw3133)
- Hannon, S., Lee, J. C., Whitmore, B. C., et al. 2019, *MNRAS*, 490, 4648, doi: [10.1093/mnras/stz2820](https://doi.org/10.1093/mnras/stz2820)
- . 2022, *MNRAS*, 512, 1294, doi: [10.1093/mnras/stac550](https://doi.org/10.1093/mnras/stac550)
- Heiles, C. 1984, *ApJS*, 55, 585, doi: [10.1086/190970](https://doi.org/10.1086/190970)
- Hensley, B. S., & Draine, B. T. 2021, *ApJ*, 906, 73, doi: [10.3847/1538-4357/abc8f1](https://doi.org/10.3847/1538-4357/abc8f1)
- Jeffreson, S. M. R., Krumholz, M. R., Fujimoto, Y., et al. 2021, *MNRAS*, 505, 3470, doi: [10.1093/mnras/stab1536](https://doi.org/10.1093/mnras/stab1536)
- Joye, W. A., & Mandel, E. 2003, in *Astronomical Society of the Pacific Conference Series*, Vol. 295, Astronomical Data Analysis Software and Systems XII, ed. H. E. Payne, R. I. Jedrzejewski, & R. N. Hook, 489
- Kannan, R., Marinacci, F., Simpson, C. M., Glover, S. C. O., & Hernquist, L. 2020, *MNRAS*, 491, 2088, doi: [10.1093/mnras/stz3078](https://doi.org/10.1093/mnras/stz3078)
- Keller, B. W., Kruijssen, J. M. D., & Chevance, M. 2022, *MNRAS*, 514, 5355, doi: [10.1093/mnras/stac1607](https://doi.org/10.1093/mnras/stac1607)
- Keller, B. W., Wadsley, J., Benincasa, S. M., & Couchman, H. M. P. 2014, *MNRAS*, 442, 3013, doi: [10.1093/mnras/stu1058](https://doi.org/10.1093/mnras/stu1058)
- Keller, B. W., Wadsley, J., & Couchman, H. M. P. 2015, *MNRAS*, 453, 3499, doi: [10.1093/mnras/stv1789](https://doi.org/10.1093/mnras/stv1789)
- . 2016, *MNRAS*, 463, 1431, doi: [10.1093/mnras/stw2029](https://doi.org/10.1093/mnras/stw2029)
- Kennicutt, Robert C., J., Armus, L., Bendo, G., et al. 2003, *PASP*, 115, 928, doi: [10.1086/376941](https://doi.org/10.1086/376941)
- Kim, C.-G., & Ostriker, E. C. 2015, *ApJ*, 802, 99, doi: [10.1088/0004-637X/802/2/99](https://doi.org/10.1088/0004-637X/802/2/99)
- Kim, J., Chevance, M., Kruijssen, J. M. D., et al. 2021a, *MNRAS*, 504, 487, doi: [10.1093/mnras/stab878](https://doi.org/10.1093/mnras/stab878)
- . 2022, *MNRAS*, 516, 3006, doi: [10.1093/mnras/stac2339](https://doi.org/10.1093/mnras/stac2339)
- Kim, J.-G., Kim, W.-T., & Ostriker, E. C. 2018, *ApJ*, 859, 68, doi: [10.3847/1538-4357/aabe27](https://doi.org/10.3847/1538-4357/aabe27)
- Kim, J.-G., Ostriker, E. C., & Filippova, N. 2021b, *ApJ*, 911, 128, doi: [10.3847/1538-4357/abe934](https://doi.org/10.3847/1538-4357/abe934)
- Krause, M. G. H., Diehl, R., Bagetakos, Y., et al. 2015, *A&A*, 578, A113, doi: [10.1051/0004-6361/201525847](https://doi.org/10.1051/0004-6361/201525847)
- Kruijssen, J. M. D., Schrubba, A., Chevance, M., et al. 2019, *Nature*, 569, 519, doi: [10.1038/s41586-019-1194-3](https://doi.org/10.1038/s41586-019-1194-3)
- Krumholz, M. R., Bate, M. R., Arce, H. G., et al. 2014, in *Protostars and Planets VI*, ed. H. Beuther, R. S. Klessen, C. P. Dullemond, & T. Henning, 243, doi: [10.2458/azu_uapress.9780816531240-ch011](https://doi.org/10.2458/azu_uapress.9780816531240-ch011)
- Lang, P., Meidt, S. E., Rosolowsky, E., et al. 2020, *ApJ*, 897, 122, doi: [10.3847/1538-4357/ab9953](https://doi.org/10.3847/1538-4357/ab9953)
- Lee, J., et al. subm., *ApJL*
- Lee, J. C., Whitmore, B. C., Thilker, D. A., et al. 2022, *ApJS*, 258, 10, doi: [10.3847/1538-4365/ac1fe5](https://doi.org/10.3847/1538-4365/ac1fe5)
- Leroy, A., et al. subm., *ApJL*
- Leroy, A. K., Walter, F., Sandstrom, K., et al. 2013, *AJ*, 146, 19, doi: [10.1088/0004-6256/146/2/19](https://doi.org/10.1088/0004-6256/146/2/19)
- Leroy, A. K., Sandstrom, K. M., Lang, D., et al. 2019, *ApJS*, 244, 24, doi: [10.3847/1538-4365/ab3925](https://doi.org/10.3847/1538-4365/ab3925)
- Leroy, A. K., Schinnerer, E., Hughes, A., et al. 2021a, *arXiv e-prints*, arXiv:2104.07739. <https://arxiv.org/abs/2104.07739>
- Leroy, A. K., Hughes, A., Liu, D., et al. 2021b, *ApJS*, 255, 19, doi: [10.3847/1538-4365/abec80](https://doi.org/10.3847/1538-4365/abec80)
- Leroy, A. K., Schinnerer, E., Hughes, A., et al. 2021, PHANGS-ALMA: Arcsecond CO(2-1) Imaging of Nearby Star-Forming Galaxies

- Li, A. 2020, *Nature Astronomy*, 4, 339, doi: [10.1038/s41550-020-1051-1](https://doi.org/10.1038/s41550-020-1051-1)
- Mac Low, M.-M., & McCray, R. 1988, *ApJ*, 324, 776, doi: [10.1086/165936](https://doi.org/10.1086/165936)
- Martizzi, D., Faucher-Giguère, C.-A., & Quataert, E. 2015, *MNRAS*, 450, 504, doi: [10.1093/mnras/stv562](https://doi.org/10.1093/mnras/stv562)
- McKee, C. F., & Ostriker, J. P. 1977, *ApJ*, 218, 148, doi: [10.1086/155667](https://doi.org/10.1086/155667)
- McLeod, A. F., Ali, A. A., Chevance, M., et al. 2021, *MNRAS*, 508, 5425, doi: [10.1093/mnras/stab2726](https://doi.org/10.1093/mnras/stab2726)
- Nath, B. B., Das, P., & Oey, M. S. 2020, *Monthly Notices of the Royal Astronomical Society*, 493, 1034, doi: [10.1093/mnras/staa336](https://doi.org/10.1093/mnras/staa336)
- Oey, M. S., & Clarke, C. J. 1997, *Monthly Notices of the Royal Astronomical Society*, 289, 570, doi: [10.1093/mnras/289.3.570](https://doi.org/10.1093/mnras/289.3.570)
- Orr, M. E., Fielding, D. B., Hayward, C. C., & Burkhart, B. 2022, *The Astrophysical Journal Letters*, 924, L28, doi: [10.3847/2041-8213/ac479f](https://doi.org/10.3847/2041-8213/ac479f)
- Palous, J., Franco, J., & Tenorio-Tagle, G. 1990, *A&A*, 227, 175
- Pettitt, A. R., Tasker, E. J., Wadsley, J. W., Keller, B. W., & Benincasa, S. M. 2017, *MNRAS*, 468, 4189, doi: [10.1093/mnras/stx736](https://doi.org/10.1093/mnras/stx736)
- Pineda, J. E., Arzoumanian, D., André, P., et al. 2022, *arXiv e-prints*, arXiv:2205.03935. <https://arxiv.org/abs/2205.03935>
- Querejeta, M., Meidt, S. E., Schinnerer, E., et al. 2015, *ApJS*, 219, 5, doi: [10.1088/0067-0049/219/1/5](https://doi.org/10.1088/0067-0049/219/1/5)
- Rahner, D., Pellegrini, E. W., Glover, S. C. O., & Klessen, R. S. 2017, *MNRAS*, 470, 4453, doi: [10.1093/mnras/stx1532](https://doi.org/10.1093/mnras/stx1532)
- . 2019, *MNRAS*, 483, 2547, doi: [10.1093/mnras/sty3295](https://doi.org/10.1093/mnras/sty3295)
- Raskutti, S., Ostriker, E. C., & Skinner, M. A. 2016, *ApJ*, 829, 130, doi: [10.3847/0004-637X/829/2/130](https://doi.org/10.3847/0004-637X/829/2/130)
- Regan, M. W., Thornley, M. D., Vogel, S. N., et al. 2006, *ApJ*, 652, 1112, doi: [10.1086/505382](https://doi.org/10.1086/505382)
- Robitaille, T. 2019, *APLpy v2.0: The Astronomical Plotting Library in Python*, doi: [10.5281/zenodo.2567476](https://doi.org/10.5281/zenodo.2567476)
- Robitaille, T., & Bressert, E. 2012, *APLpy: Astronomical Plotting Library in Python*, *Astrophysics Source Code Library*. <http://ascl.net/1208.017>
- Sandstrom, K., et al. *subm.*, *ApJL*
- Sharma, P., Roy, A., Nath, B. B., & Shchekinov, Y. 2014, *MNRAS*, 443, 3463, doi: [10.1093/mnras/stu1307](https://doi.org/10.1093/mnras/stu1307)
- Simpson, R. J., Povich, M. S., Kendrew, S., et al. 2012, *MNRAS*, 424, 2442, doi: [10.1111/j.1365-2966.2012.20770.x](https://doi.org/10.1111/j.1365-2966.2012.20770.x)
- Smith, J. D. T., Draine, B. T., Dale, D. A., et al. 2007, *ApJ*, 656, 770, doi: [10.1086/510549](https://doi.org/10.1086/510549)
- Sun, J., Leroy, A. K., Ostriker, E. C., et al. 2020, *ApJ*, 892, 148, doi: [10.3847/1538-4357/ab781c](https://doi.org/10.3847/1538-4357/ab781c)
- Tamburro, D., Rix, H. W., Leroy, A. K., et al. 2009, *AJ*, 137, 4424, doi: [10.1088/0004-6256/137/5/4424](https://doi.org/10.1088/0004-6256/137/5/4424)
- Teyssier, R. 2002, *A&A*, 385, 337, doi: [10.1051/0004-6361:20011817](https://doi.org/10.1051/0004-6361:20011817)
- Thornton, K., Gaudlitz, M., Janka, H. T., & Steinmetz, M. 1998, *ApJ*, 500, 95, doi: [10.1086/305704](https://doi.org/10.1086/305704)
- Tress, R. G., Smith, R. J., Sormani, M. C., et al. 2020, *MNRAS*, 492, 2973, doi: [10.1093/mnras/stz3600](https://doi.org/10.1093/mnras/stz3600)
- Tress, R. G., Sormani, M. C., Smith, R. J., et al. 2021, *MNRAS*, 505, 5438, doi: [10.1093/mnras/stab1683](https://doi.org/10.1093/mnras/stab1683)
- Veilleux, S., Cecil, G., & Bland-Hawthorn, J. 2005, *ARA&A*, 43, 769, doi: [10.1146/annurev.astro.43.072103.150610](https://doi.org/10.1146/annurev.astro.43.072103.150610)
- Wada, K. 2008, *ApJ*, 675, 188, doi: [10.1086/525037](https://doi.org/10.1086/525037)
- Walter, F., Brinks, E., de Blok, W. J. G., et al. 2008, *AJ*, 136, 2563, doi: [10.1088/0004-6256/136/6/2563](https://doi.org/10.1088/0004-6256/136/6/2563)
- Watkins, E., et al. *subm.*, *ApJL*
- Watson, C., Povich, M. S., Churchwell, E. B., et al. 2008, *ApJ*, 681, 1341, doi: [10.1086/588005](https://doi.org/10.1086/588005)
- Weaver, R., McCray, R., Castor, J., Shapiro, P., & Moore, R. 1977, *ApJ*, 218, 377, doi: [10.1086/155692](https://doi.org/10.1086/155692)
- Weisz, D. R., Skillman, E. D., Cannon, J. M., et al. 2009a, *ApJ*, 704, 1538, doi: [10.1088/0004-637X/704/2/1538](https://doi.org/10.1088/0004-637X/704/2/1538)
- . 2009b, *ApJL*, 691, L59, doi: [10.1088/0004-637X/691/1/L59](https://doi.org/10.1088/0004-637X/691/1/L59)
- Whitworth, A. P., Bhattal, A. S., Chapman, S. J., Disney, M. J., & Turner, J. A. 1994, *MNRAS*, 268, 291, doi: [10.1093/mnras/268.1.291](https://doi.org/10.1093/mnras/268.1.291)
- Zucker, C., Goodman, A. A., Alves, J., et al. 2022, *Nature*, 601, 334, doi: [10.1038/s41586-021-04286-5](https://doi.org/10.1038/s41586-021-04286-5)

All Authors and Affiliations

ASHLEY. T. BARNES ^{1,2} ELIZABETH J. WATKINS ³ SHARON E. MEIDT ⁴ KATHRYN KRECKEL ³ MATTIA C. SORMANI ⁵ ROBIN G. TRESS ⁶
SIMON C. O. GLOVER ⁵ FRANK BIGIEL ⁷ RUPALI CHANDAR ⁸ ERIC Emsellem ^{2,9} JANICE C. LEE ¹⁰ ADAM K. LEROY ^{11,12}
KARIN M. SANDSTROM ¹³ EVA SCHINNERER ¹⁴ ERIK ROSOLOWSKY ¹⁵ FRANCESCO BELFIORE ¹⁶ GUILLERMO A. BLANC ^{17,18}
MÉDÉRIC BOQUIEN ¹⁹ JAKOB DEN BROK ¹ YIXIAN CAO ²⁰ MÉLANIE CHEVANCE ^{5,21} DANIEL A. DALE ²² OLEG V. EGOROV ³
COSIMA EIBENSTEINER ²³ KATHRYN GRASHA ^{24,25} BRENT GROVES ²⁶ HAMID HASSANI ¹⁵ JONATHAN D. HENSHAW ^{27,14}
SARAH JEFFRESON ²⁸ MARÍA J. JIMÉNEZ-DONAIRE ²⁹ BENJAMIN W. KELLER ³⁰ RALF S. KLESSEN ^{5,31} ERIC W. KOCH ³²
J. M. DIEDERIK KUIJSSSEN ²¹ KIRSTEN L. LARSON ³³ JING LI ³ DAIZHONG LIU ²⁰ LAURA A. LOPEZ ^{11,12,34} ERIC J. MURPHY ³⁵
LUKAS NEUMANN ¹ JÉRÔME PÉTY ^{36,37} FRANCESCA PINNA ¹⁴ MIGUEL QUEREJETA ²⁹ FLORENT RENAUD ³⁸ TOSHIKI SAITO ³⁹
SUMIT K. SARBADHICARY ^{11,12} AMY SARDONE ⁴⁰ ROWAN J. SMITH ⁴¹ SOPHIA K. STUBER ¹⁴ JIAYI SUN ^{42,43} DAVID A. THILKER ⁴⁴
ANTONIO USERO ²⁹ BRADLEY C. WHITMORE ⁴⁵ AND THOMAS G. WILLIAMS ^{46,14}

¹Argelander-Institut für Astronomie, Universität Bonn, Auf dem Hügel 71, 53121, Bonn, Germany

²European Southern Observatory, Karl-Schwarzschild-Straße 2, 85748 Garching, Germany

³Astronomisches Rechen-Institut, Zentrum für Astronomie der Universität Heidelberg, Mönchhofstraße 12-14, 69120 Heidelberg, Germany

⁴Sterrenkundig Observatorium, Universiteit Gent, Krijgslaan 281 S9, B-9000 Gent, Belgium

⁵Universität Heidelberg, Zentrum für Astronomie, Institut für Theoretische Astrophysik, Albert-Ueberle-Straße 2, D-69120 Heidelberg, Germany

⁶Institute of Physics, Laboratory for galaxy evolution and spectral modelling, EPFL, Observatoire de Sauverny, Chemin Pegais 51, 1290 Versoix, Switzerland.

⁷Argelander-Institut für Astronomie, Universität Bonn, Auf dem Hügel 71, 53121 Bonn, Germany

⁸Ritter Astrophysical Research Center, University of Toledo, Toledo, OH 43606, USA

⁹Univ Lyon, Univ Lyon1, ENS de Lyon, CNRS, Centre de Recherche Astrophysique de Lyon UMR5574, F-69230 Saint-Genis-Laval France

¹⁰Gemini Observatory/NSF's NOIRLab, 950 N. Cherry Avenue, Tucson, AZ, 85719, USA

¹¹Department of Astronomy, The Ohio State University, 140 West 18th Avenue, Columbus, Ohio 43210, USA

¹²Center for Cosmology and Astroparticle Physics, 191 West Woodruff Avenue, Columbus, OH 43210, USA

¹³Department of Physics, University of California, San Diego, 9500 Gilman Drive, San Diego, CA 92093, USA

¹⁴Max-Planck-Institut für Astronomie, Königstuhl 17, D-69117 Heidelberg, Germany

¹⁵Department of Physics, University of Alberta, Edmonton, Alberta, T6G 2E1, Canada

¹⁶INAF — Arcetri Astrophysical Observatory, Largo E. Fermi 5, I-50125, Florence, Italy

¹⁷The Observatories of the Carnegie Institution for Science, 813 Santa Barbara St., Pasadena, CA, USA

¹⁸Departamento de Astronomía, Universidad de Chile, Camino del Observatorio 1515, Las Condes, Santiago, Chile

¹⁹Centro de Astronomía (CITEVA), Universidad de Antofagasta, Avenida Angamos 601, Antofagasta, Chile

²⁰Max-Planck-Institut für Extraterrestrische Physik (MPE), Giessenbachstr. 1, D-85748 Garching, Germany

²¹Cosmic Origins Of Life (COOL) Research DAO, coolresearch.io

²²Department of Physics and Astronomy, University of Wyoming, Laramie, WY 82071, USA

²³Argelander-Institut für Astronomie, Universität Bonn, Auf dem Hügel 71, 53121 Bonn, Germany

²⁴Research School of Astronomy and Astrophysics, Australian National University, Canberra, ACT 2611, Australia

²⁵ARC center of Excellence for All Sky Astrophysics in 3 Dimensions (ASTRO 3D), Australia

²⁶International center for Radio Astronomy Research, University of Western Australia, 7 Fairway, Crawley, 6009 WA, Australia

²⁷Astrophysics Research Institute, Liverpool John Moores University, 146 Brownlow Hill, Liverpool L3 5RF, UK

²⁸Center for Astrophysics, Harvard & Smithsonian

²⁹Observatorio Astronómico Nacional (IGN), C/Alfonso XII, 3, E-28014 Madrid, Spain

³⁰Department of Physics and Materials Science, University of Memphis, 3720 Alumni Avenue, Memphis, TN 38152, USA

³¹Universität Heidelberg, Interdisziplinäres Zentrum für Wissenschaftliches Rechnen, Im Neuenheimer Feld 205, D-69120 Heidelberg, Germany

³²Center for Astrophysics — Harvard & Smithsonian, 60 Garden St., 02138 Cambridge, MA, USA

³³AURA for the European Space Agency (ESA), Space Telescope Science Institute, 3700 San Martin Drive, Baltimore, MD 21218, USA

³⁴Flatiron Institute, Center for Computational Astrophysics, NY 10010, USA

³⁵National Radio Astronomy Observatory, 520 Edgemont Road, Charlottesville, VA 22903, USA

³⁶IRAM, 300 rue de la Piscine, 38400 Saint Martin d'Hères, France

³⁷LERMA, Observatoire de Paris, PSL Research University, CNRS, Sorbonne Universités, 75014 Paris

³⁸Department of Astronomy and Theoretical Physics, Lund Observatory, Box 43, SE-221 00 Lund, Sweden

³⁹National Astronomical Observatory of Japan, 2-21-1 Osawa, Mitaka, Tokyo, 181-8588, Japan

⁴⁰Department of Astronomy, The Ohio State University, 140 West 18th Avenue, Columbus, OH 43210, USA

⁴¹Jodrell Bank center for Astrophysics, Department of Physics and Astronomy, University of Manchester, Oxford Road, Manchester M13 9PL, UK

⁴²Department of Physics and Astronomy, McMaster University, 1280 Main Street West, Hamilton, ON L8S 4M1, Canada

⁴³Canadian Institute for Theoretical Astrophysics (CITA), University of Toronto, 60 St George Street, Toronto, ON M5S 3H8, Canada

⁴⁴Department of Physics and Astronomy, The Johns Hopkins University, Baltimore, MD 21218, USA

⁴⁵*Space Telescope Science Institute, 3700 San Martin Drive, Baltimore, MD, USA*

⁴⁶*Sub-department of Astrophysics, Department of Physics, University of Oxford, Keble Road, Oxford OX1 3RH, UK*